



The Tim8–Tim13 Complex Has Multiple Substrate Binding Sites and Binds Cooperatively to Tim23

Kristen N. Beverly¹, Michael R. Sawaya², Einhard Schmid¹
and Carla M. Koehler^{1*}

¹Department of Chemistry and Biochemistry, Box 951569, University of California, Los Angeles, CA 90095-1569, USA

²Howard Hughes Medical Institute, UCLA-DOE Institute of Genomics and Proteomics, Los Angeles, CA 90095-1570, USA

Received 27 April 2008;
received in revised form
22 July 2008;
accepted 24 July 2008
Available online
30 July 2008

The Tim8–Tim13 complex, located in the mitochondrial intermembrane space, functions in the TIM22 import pathway that mediates the import of the mitochondrial carriers Tim23, Tim22, and Tim17 into the mitochondrial inner membrane. The Tim8–Tim13 complex assembles as a hexamer and binds to the substrate Tim23 to chaperone the hydrophobic Tim23 across the aqueous intermembrane space. However, both structural features of the Tim8–Tim13 complex and the binding interaction to Tim23 remain poorly defined. The crystal structure of the yeast Tim8–Tim13 complex, reported here at 2.6 Å resolution, reveals that the architecture of the Tim8–Tim13 complex is similar to those of other chaperones such as Tim9–Tim10, prefoldin, and Skp, in which long helices extend from a central body like tentacles from a jellyfish. Surface plasmon resonance was applied to investigate interactions between the Tim8–Tim13 complex and Tim23. The Tim8–Tim13 complex contained approximately six binding sites and showed a complex binding interaction indicative of positive cooperativity rather than a simple bimolecular interaction. By combining results from the structural and binding studies, we provide a molecular model of the Tim8–Tim13 complex binding to Tim23. The regions where the tentacle helices attach to the body of the Tim8–Tim13 complex contain six hydrophobic pockets that likely interact with specific sequences of Tim23 and possibly other substrates. Smaller hydrophobic patches on the tentacles themselves likely interact nonspecifically with the substrate's transmembrane helices, shielding it from the aqueous intermembrane space. The central region of Tim23, which enters the intermembrane space first, may serve to nucleate the binding of the Tim8–Tim13 complex, thereby initiating the chaperoned translocation of Tim23 to the mitochondrial inner membrane.

© 2008 Elsevier Ltd. All rights reserved.

Keywords: mitochondria; protein translocation; surface plasmon resonance; cooperativity; chaperone

Edited by R. Huber

Introduction

The mitochondrion has developed an elaborate translocation system with translocons on both mitochondrial outer membrane and mitochondrial inner membrane;^{1–3} proteins destined for the mitochondrion, termed *precursors* until they reach their correct location, utilize Translocase of the Outer

Membrane (TOM) and Translocase of the Inner Membrane (TIM) complexes TIM23 and TIM22 to cross the outer and inner membranes, respectively. Proteins with a typical N-terminal targeting sequence use the TIM23 translocation system, whereas proteins destined for the inner membrane use the TIM22 translocation system. Components in the TIM22 translocation system include the small Tim proteins (Tim8, Tim9, Tim10, Tim12, and Tim13) and the membrane components Tim18, Tim22, and Tim54. The small Tim proteins assemble in hexameric complexes (referred to as small Tim complexes) in the intermembrane space in which three Tim9 polypeptides partner with three Tim10 polypeptides, and three Tim8 polypeptides partner with three Tim13 polypeptides. The insertion complex in

*Corresponding author. E-mail address: koehler@chem.ucla.edu.

Abbreviations used: TOM, Translocase of the Outer Membrane; TIM, Translocase of the Inner Membrane; AAC, ADP/ATP carrier; SPR, surface plasmon resonance; RU, resonance units; PDB, Protein Data Bank.

the inner membrane consists of a fraction of the Tim9 and Tim10 with Tim12 and membrane proteins Tim18, Tim22, and Tim54.

The TIM22 translocation system functions through the coordinated action of the Tim8–Tim13 and Tim9–Tim10 complexes and the insertion complex in the inner membrane. The substrates of the TIM22 translocation system include the mitochondrial carrier proteins and import components Tim17, Tim22, and Tim23. These substrates cross the TOM complex as a loop in an unfolded state.^{4,5} The small Tim complex Tim8–Tim13 or Tim9–Tim10 then binds to the substrates to facilitate transport across the intermembrane space. Because the intermembrane space is an aqueous compartment and the substrate is unfolded, the small Tim proteins act as chaperones to maintain the hydrophobic substrates in an import-competent state, akin to cytosolic chaperones. At the inner membrane, the small Tim complexes hand the substrate over to the insertion complex. Tim22 of the insertion complex can form a channel,⁶ and insertion of the inner membrane proteins requires a membrane potential.

The Tim8–Tim13 and Tim9–Tim10 complexes display different substrate binding preferences. The Tim9–Tim10 complex can be efficiently cross-linked to carrier proteins [such as the ADP/ATP carrier (AAC) and the phosphate carrier] and the import components Tim17, Tim23, and Tim22.^{7–9} The Tim8–Tim13 complex can be crosslinked to Tim23 and aspartate–glutamate carriers.^{7–10} Peptide scans have also been utilized to determine the binding specificity of the small Tim complexes for different substrates. As reported, peptide scans for the carriers and for Tim23 were developed, in which 13-mer peptides (overlapping by 10 amino acids) for the entire sequence of the query protein were sequentially spotted on membranes; the membranes were used for far-Western analysis with the small Tim complexes.¹¹ These assays showed that the Tim9–Tim10 and Tim8–Tim13 complexes bound specifically to several regions in representative substrates AAC and Tim23, respectively.^{4,11,12} Tim23 contains an N-terminal hydrophilic domain (residues 1–102), followed by four predicted membrane-spanning segments (residues 103–120, 153–160, 171–191, and 200–210). The Tim8–Tim13 complex showed the most robust binding to amino acids 80–102 of the N-terminal hydrophilic domain, as well as binding to the N-terminal side of the transmembrane domains. In addition, the results from the peptide scans were supported by a recent crosslinking study in which cysteine residues were engineered into Tim23; Tim8 preferentially bound to amino acids 80–90 in the N-terminal hydrophilic domain, and Tim13 preferentially bound to transmembrane domain 2 (residues 155–160).^{9,13} This study also showed that the Tim8–Tim13 complex bound to several sites throughout Tim23,^{9,13} as was reported in the peptide scan experiments.

Recently, the crystal structure of the *Saccharomyces cerevisiae* Tim9–Tim10 complex showed that it was similar to that of the *Methanobacterium thermoauto-*

trophicum prefoldin and *Escherichia coli* Skp chaperone,^{14–17} although the complexes were not similar at the sequence level. The Tim9–Tim10 complex assembles as a hexamer consisting of a trimer of Tim9–Tim10 dimers.¹⁷ The bacterial Skp chaperone assembles as a trimeric periplasmic chaperone that assists outer membrane proteins in their folding and insertion into membranes,¹⁴ whereas prefoldin is a hexameric chaperone built from two related classes of subunits that functions in the cytosol of all eukaryotes and archaea to stabilize nonnative proteins.¹⁵ In each of these chaperones, long helices extend from a central body like tentacles from a jellyfish.^{14,15} In this study, we have determined the structure of the Tim8–Tim13 complex at 2.6 Å and show that it is similar to that of Tim9–Tim10.¹⁷ The structural analysis has offered some clues about potential substrate binding sites for Tim23. Presumably, the helices assist in protein folding by providing a cavity in which nonnative polypeptides can be enclosed and protected against intermolecular aggregation. In addition, there are six hydrophobic pockets where the tentacle helices attach to the body of the Tim8–Tim13 hexamer, providing specificity for substrate binding.

Crosslinking and peptide scan analysis showed that binding interactions between the small Tim proteins and substrates were specific. We therefore have also used surface plasmon resonance (SPR) to investigate the molecular interactions of both the Tim13 monomer and the Tim8–Tim13 complex with peptides derived from Tim23. Based on the crystal structure and these binding studies, we present a molecular model of the Tim8–Tim13 complex's binding to Tim23 and suggest that the Tim8–Tim13 complex undergoes conformational changes to induce high-affinity multivalent substrate binding.

Results

The Tim8–Tim13 structure is similar to the Tim9–Tim10 structure

The Tim8–Tim13 complex was produced for structure determination by coexpressing the Tim8–Tim13 complex from a single transcript in *E. coli* and by purifying the recombinant complex to greater than 95% purity using chromatography, as described previously.⁴ Initial crystals were obtained from sparse matrix crystal screening kits, followed by customized fine-grid optimization. Diffraction from the best of these crystals was anisotropic, ranging between 3.1 and 2.5 Å resolution. The phase problem was solved using molecular replacement with a Tim8–Tim13 homology model as search model. The homology model was based on the published Tim9–Tim10 complex.¹⁷ The asymmetric unit of the Tim8–Tim13 crystal contained two hexamers. The structure was refined to $R_{\text{work}} = 24.2\%$ and $R_{\text{free}} = 29.1\%$ (Table 1). Several N-terminal residues and a few C-terminal residues were invisible on the electron density map

Table 1. Statistics of X-ray data collection and atomic refinement

	P1
Space group	P1
Unit cell parameters	
<i>a</i> , <i>b</i> , <i>c</i> (Å)	55.7, 56.3, 59.8
α , β , γ (°)	89.1, 89.7, 60.3
Resolution range (Å)	90.0–2.60 (2.6–2.7)
R_{sym}^a (%)	8.6 (37.8)
Number of unique data	19,026 (1882)
Number of unique data after ellipsoidal truncation	13,863 (285)
Completeness of data (%)	96.0 (94.1)
Completeness of data after ellipsoidal truncation (%)	75.6 (20.0)
$I/\sigma(I)$	11.4 (2.4)
Number of residues	664
(12 chains/asymmetric unit)	
Number of protein atoms	5299
Number of solvent atoms	18
Matthews' coefficient (Å ³ /Da) ^b	2.2
R (%) ^c	24.6
R_{free} (%) ^d	29.0
Test set size (%) (selection)	5.3 (random)
RMSD from target values	
Bond lengths (Å)	0.014
Bond angles (°)	1.4
Average <i>B</i> -factor for main-chain atoms	22.3
Average <i>B</i> -factor for side-chain atoms	26.1
RMS <i>B</i> -factor for main-chain atoms	1.0
RMS <i>B</i> -factor for side-chain atoms	3.0
PDB deposition ID code	3CJH

Numbers in parentheses refer to the outer shell of the data.

^a $R_{\text{sym}} = \sum |I_o - I_o(\text{mean})|^2 / \sum [I_o^2]$, where F_o is the observed structure factor. Both summations involve all input reflections for which more than one symmetry equivalent is averaged.

^b Matthews' coefficient as defined by Matthews.¹⁸

^c $R = \sum |F_o| - |F_c| / \sum |F_o|$.

^d R_{free} as defined by Brünger.¹⁹

due to disorder. These include Tim8 residues 1–27 and 87 and Tim13 residues 1–45 and 98–104. A similar extent of disorder was observed in the crystal structure of Tim9–Tim10, where residues 1–12 and 86–89 were disordered in Tim9, and where residues 1–12 and 78–90 were disordered in Tim10.¹⁷ The disorder could be a natural consequence of the lack of substrate in the crystal structure (see below).

Overall, Tim8–Tim13 and Tim9–Tim10 complexes are structurally similar. The Tim fold consists of a pair of antiparallel helices joined by two disulfide bonds and a connecting loop. The four types of Tim molecules (Tim8, Tim9, Tim10, and Tim13) are structurally superimposable over 42–58 C α pairs, with no pairwise RMSD greater than 1.5 Å (Table 2), despite sharing less than 25% sequence identity in any pairwise comparison (Fig. 1). Three Tim8 molecules and three Tim13 molecules nestle alternately around a heterohexameric barrel, giving the barrel 3-fold rotational symmetry (pseudo-6-fold rotational symmetry) (Fig. 1). The N-terminal helices line the inside of the barrel, and the C-terminal helices line the outside of the barrel. The geometry is analogous to the Tim9–Tim10 complex. In fact, the two heterohexameric complexes can be superimposed with an RMSD of only 1.9 Å over 314 C α pairs. Distinctively, the N- and C-terminal helices project from one end of this barrel core like tentacles from a

jellyfish (Fig. 1b).^{14,15} This architecture grossly resembles those of prefoldin and Skp chaperones, in which amphiphilic helical tentacles emanate from an umbrella-like β -sheet domain.^{22,23} These tentacle regions are implicated in sequestering substrate from aggregation. The disorder observed at the tips of these tentacles (extreme N- and C-termini) in the Tim8–Tim13 and Tim9–Tim10 complexes could be the result of a lack of substrate molecule to lend an interaction surface.

The greatest structural difference between Tim8–Tim13 and Tim9–Tim10 complexes lies in the positions and lengths of their terminal helices (i.e., tentacles). Tim8 and Tim13 sequences have 12 and 30 more residues preceding the barrel compared to Tim9 and Tim10 (Fig. 1c). Conversely, Tim9 and Tim10 sequences have 9 and 17 more residues following the barrel compared to Tim8 and Tim13 (Fig. 1c). Although the extra N-terminal residues are largely disordered in the Tim8–Tim13 crystal structure, they presumably extend farther away from the barrel—partially helical, partially random coil. Notably, the N-terminal helices sit on the inner perimeter of the barrel, 12 Å closer to the center of the barrel than the C-terminal helices sitting on the outer perimeter of the barrel. It follows that these N-terminal tentacles of Tim8–Tim13 would be in closer proximity to each other compared to the C-terminal tentacles of Tim9–Tim10. If these tentacles function to encompass the substrate molecule (as has been suggested for the similarly shaped prefoldin molecule^{22,23}), the relative differences in the positions of these tentacles suggest that Tim8–Tim13 would prefer smaller substrates to the Tim9–Tim10 tentacles. Sequence alignments of Tim13 and Tim8 proteins show variability in tentacle lengths, suggesting that such size preferences might vary among species.

Hydrophobic patches on Tim8–Tim13 suggest a mechanism for achieving substrate specificity

Over the surface of the hexameric barrel, Tim8–Tim13 and Tim9–Tim10 share similar patches of hydrophobicity. Most of the barrel's surface is hydrophilic, including the pore in the center of the barrel, making these areas unlikely candidates for substrate interactions. But a relatively large hydrophobic region can be found where the tentacles join the barrel. This side of the barrel contains six hydrophobic cavities composed of Tim8 residues Val33, Ile37, Leu73, and Leu83, and Tim13 residues Leu49, Ile53, Leu78, Tyr81, Met82, Trp85, Tyr92, and

Table 2. C α superposition of the four TIM molecules (chain A) onto one another

	Tim8	Tim9	Tim10	Tim13
Tim8		0.93 (49)	1.17 (50)	1.46 (42)
Tim9			0.71 (58)	0.92 (44)
Tim10				0.91 (43)
Tim13				

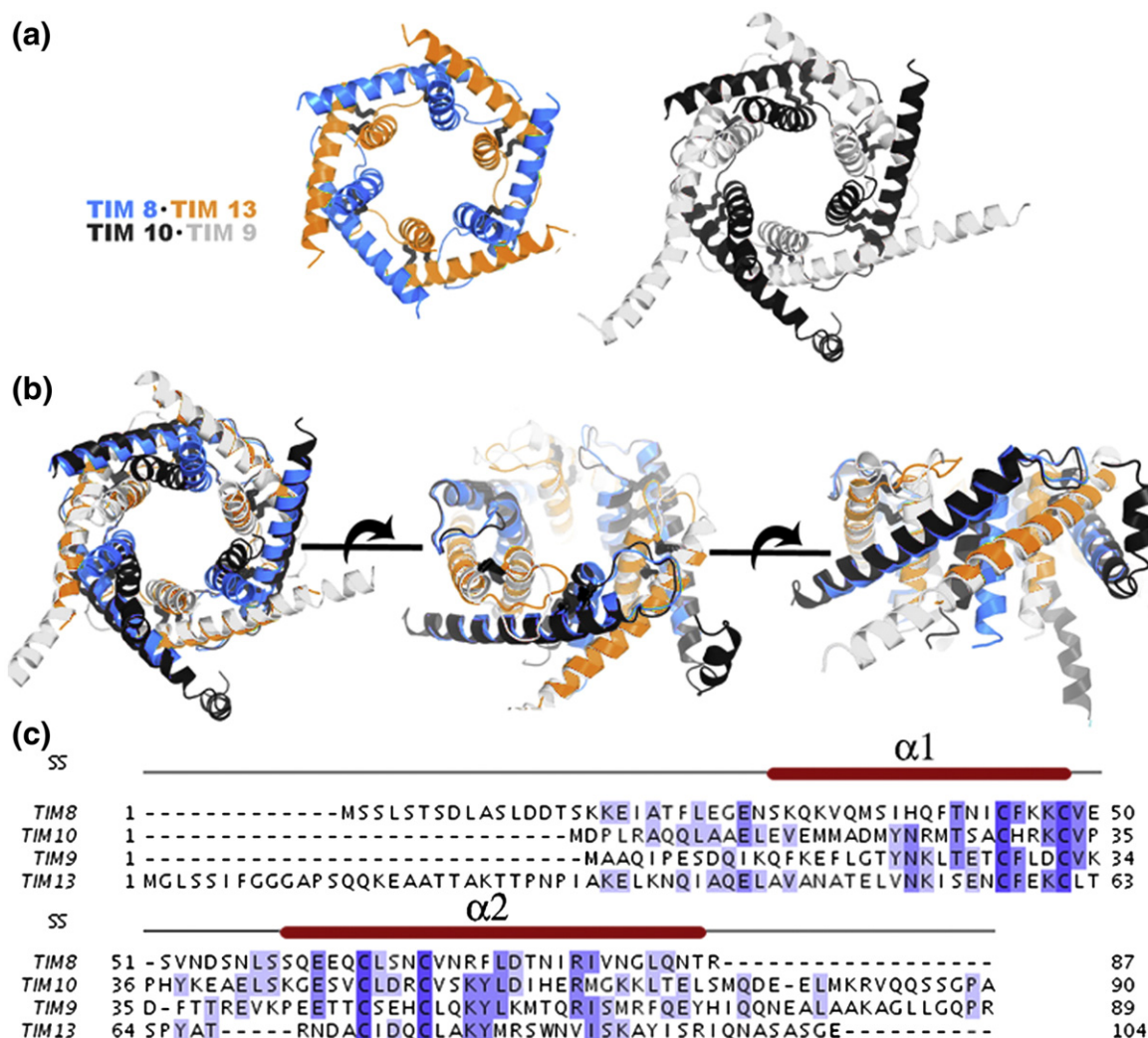


Fig. 1. Comparison of Tim8–Tim13 and Tim9–Tim10 structures. (a) Ribbon diagrams of the Tim8–Tim13 (TIM8–13) complex and the Tim9–Tim10 (TIM9–10) complex (PDB ID 2BSK) illustrate similarities in oligomeric assembly. In this view, the “tentacle” helices point toward the viewer. The largest differences appear in the N-terminal helices of Tim8 and Tim10 (blue and cyan helices lining the central pore). Red sticks indicate the location of conserved intrachain disulfide bonds. (b) Superposition of the Tim8–Tim13 and Tim9–Tim10 complexes. (c) Structure-based sequence alignment of Tim8, Tim9, Tim10, and Tim13. The secondary structure elements (top) are mapped to the four sequences. This figure was prepared using the programs Jalview²⁰ and PyMOL.²¹

Ile96 (Fig. 7a). Similar hydrophobic pockets are found in the Tim9–Tim10 complex in the same locations, although they are composed of different hydrophobic residues. The sequence differences could encode substrate specificity. Due to the curvature of these pockets, any potential interaction is probably with the substrate’s interhelical loops rather than with the transmembrane helices themselves. Additional hydrophobic patches with increased accessibility exist on the tentacles, but they are smaller. These patches are located about midway down the length of the tentacles, making them the most likely contact points with the transmembrane segments of substrate molecules. They consist of Tim8 residues Ile20, Phe23, and Leu24, and Tim13 residues Ile29, Leu33, and Ile37. These patches are interspersed with positive and negative charges similar to the tentacles of prefoldin

and Skp chaperones.^{14,15} Since the tentacle sequences are also poorly conserved among species, the amino acids forming the tentacles might also encode substrate specificity.

Molecular interactions between the Tim8–Tim13 complex and peptides derived from Tim23

To determine how the Tim8–Tim13 complex binds to a substrate, SPR analysis with the Tim8–Tim13 complex, with Tim13 monomer, and with peptides derived from Tim23 was used. Tim23 contains an N-terminal hydrophilic domain (residues 1–102), followed by four predicted membrane-spanning segments (residues 103–120, 153–160, 171–191, and 200–210). Previous biochemical studies using peptide scans have shown that the Tim8–Tim13 complex bound to distinct peptides in Tim23.⁴ Studies

by Alder *et al.* indicate that the Tim8–Tim13 complex can be readily crosslinked to residues in the C-terminal half of the hydrophilic domain of Tim23 (amino acids 80–90), among other regions.¹³ Because residues 75–110 of Tim23 (the C-terminal half of the hydrophilic domain and transmembrane domain 1) showed the strongest binding in peptide scan experiments,⁴ we predicted that this region may be translocated first into the intermembrane space and likely interact with the Tim8–Tim13 complex. We have employed SPR experiments with a BIACORE T100 instrument (BIACORE AB, Uppsala, Sweden) to investigate the molecular interactions in more detail, focusing on the aforementioned region. As a strategy, Tim13 or the Tim8–Tim13 complex was tethered to a Ni²⁺-coated sensor chip. The Tim8–Tim13 complex was coupled by a C-terminal 10× His tag on Tim8, and the Tim13 monomer was coupled by a C-terminal 10× His tag (Fig. 2a). The recombinant proteins were purified using Ni²⁺ agarose (Supplementary Fig. S1). This tethering approach allowed the assembled complexes to be coupled to the chip by a single defined linkage (i.e., via the C-terminus) with free rotation, rather than randomly coupled from covalent attachment via primary amines in the protein, which is typically used in SPR studies. In addition, the complex could

be removed and the sensor surface could be regenerated with a fresh aliquot of complex when sensor performance deteriorated. Thus, a similar sensor chip with a new active complex was assembled for individual experiments, in contrast to generating one chip with the complex covalently coupled via random lysine residues in the protein for repeated use.

On the basis of the peptide scan results, the peptides selected (Fig. 2b) were predicted to bind to the Tim8–Tim13 complex with different affinities (Table 3). Peptides pep^{77–88}, pep^{91–103}, and pep^{98–111} were derived from the C-terminal half of the hydrophilic domain (residues 1–102 in Tim23) and transmembrane domain 1; this region showed strongest binding in the peptide scan and cross-linking experiments to Tim8 and Tim13.^{4,9} Peptides pep^{136–148} and pep^{181–193} were derived from regions N-terminal to transmembrane domains 2 and 3, respectively, which showed decreased binding affinity in the peptide scan experiments.

The assembly states of the Tim8–Tim13 complex and of the Tim13 monomer were investigated by blue native gel analysis (Fig. 2c).²⁴ Like the endogenous Tim8–Tim13 complex in mitochondria, the Tim8–Tim13 complex migrated as a 70-kDa complex, but the Tim13 monomer migrated as a

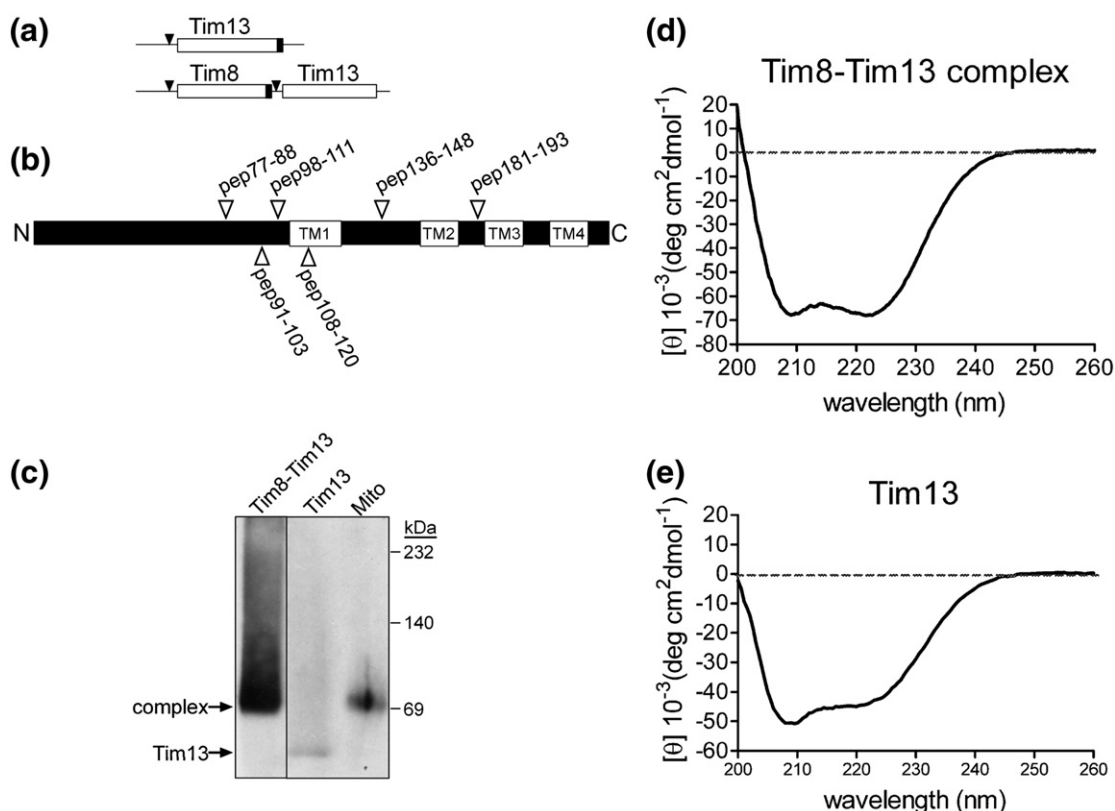


Fig. 2. The Tim8–Tim13 complex and Tim13 monomer are folded. (a) Schematic of the recombinant Tim8–Tim13 and Tim13 constructs that were purified from *E. coli*. The black box represents the location of the His tag, and the black triangle represents the ribosomal binding site. (b) Schematic showing the location of the peptides derived from Tim23. The transmembrane domains (designated TM1–TM4) are marked by white boxes. (c) Recombinant Tim8–Tim13 complex, Tim13, and a mitochondrial lysate (mito) were separated by blue native PAGE. After transfer to a polyvinylidene fluoride membrane, the membrane was blotted with a polyclonal antibody against Tim13. (d and e) CD spectral analysis shows that the recombinant Tim8–Tim13 complex and Tim13 contain mostly α -helical structures.

Table 3. Peptides derived from Tim23 for SPR studies

Tim23-derived peptide	Peptide sequence	Binding interaction from peptide scan ^a
Pep ^{77–88}	N-KREEQLSSLEGSQGLI-C	++
Pep ^{91–103}	N-KRGWTDLDCYGTGA-C	+++
Pep ^{98–111}	N-KREECYGTGAVYLLGLGI-C	+++
Pep ^{108–120}	N-KREEGLGIGGFSGMMQG-C	++
Pep ^{136–148}	N-KTVLNHITKRGPFLL-C	++
Pep ^{181–193}	N-KAGAGALTGALFKSSKG-C	++

^a Binding interaction based on peptide scan results.⁴

smaller complex. Circular dichroism (CD) analysis was used to investigate the structural properties of the monomer and the complex, as has been reported previously (Fig. 2d and e).⁴ The Tim8–Tim13 complex and Tim13 displayed similar structural properties, with approximately 70% α -helical and 6% β -sheet properties (Supplementary Fig. S1). Therefore, the Tim8–Tim13 complex was assembled, whereas the Tim13 monomer folded into a stable structure.

We first tested the Tim13 monomer in SPR studies because it is simpler than the Tim8–Tim13 complex in that it contains only one subunit of the complex. The Tim13 monomer was selected because the Tim8 monomer was problematic to purify. The Tim13 monomer was coupled to the sensor surface, and pep^{91–103} (0–500 μ M) was assayed for binding. The data for the interaction were analyzed at equilibrium using different models provided with the Scrubber-2 software; a first-order binding interaction was identified, and the saturation curve was plotted (Fig. 3). Using Eq. (1),²⁵ a binding stoichiometry of approximately 1 Tim13 polypeptide:1.5 peptides was calculated, suggesting that Tim13 may have approximately one peptide binding site. A dissociation constant K_d of 613 μ M for the Tim13h and pep^{91–103} was calculated from a Scatchard plot of the data. This analysis suggests that the Tim13 monomer indeed binds to pep^{91–103} and most likely forms a 1:1 complex.

Because we expected the complex to behave differently from the individual Tim13 monomer when binding to substrate, interactions with the Tim8–Tim13 complex were also tested to determine (a) the number of binding sites and (b) the nature of the binding interaction (i.e., bimolecular or cooperative). In the first series of SPR studies, a concentration range (0–630 μ M) of pep^{91–103} was assayed for binding to the Tim8–Tim13 complex, and a typical sensorgram is shown in Fig. 4a. Visual examination of the sensorgrams immediately showed that pep^{91–103} associated with a high on-rate and that equilibrium was reached in less than 2 s. The trace of the sensorgrams was enlarged in the range of 54–60 s to illustrate the extent of fast binding (Supplementary Fig. S2). Because the SPR instrument measures binding every 0.5 s, the on-rates for the binding of pep^{91–103} were too fast for accurate kinetic analysis; this has been documented previously.²⁶ At higher concentrations of pep^{91–103}, binding seemed to be saturated because the resonance units (RU) started

to decline quickly upon binding. As a result, equilibrium analysis was performed. The peptide was injected over 25 s, and the binding was monitored for 1.5 min. The formed complexes also quickly dissociated from the surface, and the binding curves returned to baseline in less than 1 min.

Because the binding kinetics were too fast to be measured for curve fitting, the equilibrium sensorgram values were used to plot a saturation curve (Fig. 4b). The data for the interaction were analyzed using different models provided with the Biaevaluation 3.0 and Scrubber-2 software; however, the binding curves could not be fitted in a satisfying manner to any of these models, suggesting a complex binding mode rather than the bimolecular interaction model typically observed using SPR. Indeed, the saturation curve suggested positive cooperativity. Accordingly, we used the Hill equation to model the interaction (Fig. 4c). From the Hill plot, a straight line was obtained ($r^2=0.87$). The intercept at the x -axis indicated that half saturation occurred at 393 μ M pep^{91–103}. The slope gave an estimate of the Hill coefficient (n); the coefficient was approximately 7, confirming positive cooperativity and suggesting that the Tim8–Tim13 complex contains several binding sites. As corroboration, the binding stoichiometry (Eq. (1)) ranged from 1 Tim8–Tim13 complex:5 pep^{91–103} to 1 Tim8–Tim13 complex:5.7 pep^{91–103}, also indicating that the peptide can bind to multiple sites on the Tim8–Tim13

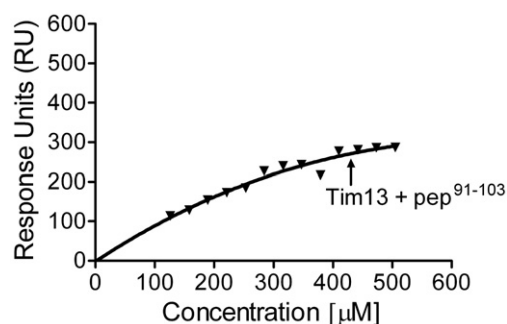


Fig. 3. Tim13 bound to pep^{91–103} in a bimolecular interaction. For SPR analysis, the Tim13 monomer was coupled to the Ni²⁺-coated sensor surface at 1500 RU. Pep^{91–103} (0–500 μ M) was analyzed for binding to the Tim13 monomer (described in Materials and Methods), and the saturation curve is shown.

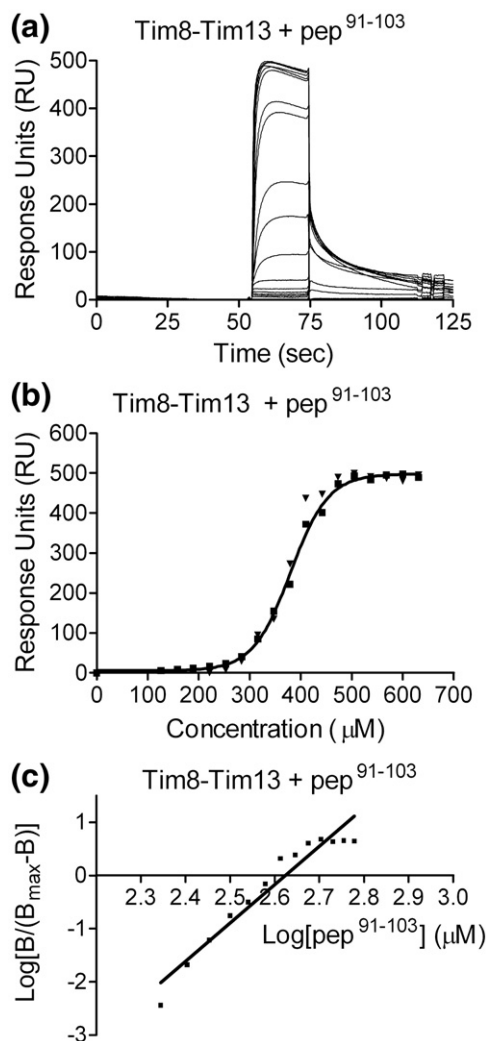


Fig. 4. Pep^{91–103} bound cooperatively to the Tim8–Tim13 complex. (a) Sensorgram showing the binding of pep^{91–103} to the Tim8–Tim13 complex. The complex was coupled to the Ni²⁺-coated sensor chip, and binding of the Tim23 pep^{91–103} [0–630 μM] was investigated (described in Materials and Methods). A representative SPR sensorgram in the ligand series is shown. (b) The kinetics of binding were too rapid for curve fitting, so the equilibrium sensorgram values from (a) (RU at equilibrium *versus* pep^{91–103} concentration) were used to plot a saturation curve. Two representative experiments are marked by triangles and squares. (c) Because the analysis from (b) did not show the expected 1:1 binding model, a Hill representation of the pep^{91–103}–Tim8–Tim13 complex association was graphed. A function of the bound pep^{91–103} [$\log B/(B_{\max}-B)$] was plotted against the logarithmic concentration of the amount of injected pep^{91–103}. The slope provides an estimate of the Hill coefficient (n), and the intercept with the x -axis provides an estimate of the concentration of free pep^{91–103} required to occupy half of the binding sites.

complex. Therefore, the Tim8–Tim13 complex has approximately six binding sites. The binding mechanism was not that of a simple bimolecular interaction, suggesting that the individual Tim subunits may acquire an increased affinity for

binding as increasing peptide binding sites are occupied.

We investigated the binding of the Tim8–Tim13 complex with other peptides derived from Tim23 (Fig. 2b), as was performed with pep^{91–103}. The binding data were plotted on a saturation graph (Fig. 5a), and the saturation data from pep^{91–103} were also included for comparison. Whereas the peptides derived from the C-terminal half of Tim23 (pep^{98–111}, pep^{108–120}, pep^{136–148}, and pep^{181–193}) did not show appreciable binding, pep^{77–88} seemed to also display cooperative binding similar to that of pep^{91–103}. The interaction between pep^{77–88} and Tim8–Tim13 was analyzed with the Hill equation (Fig. 5b), and pep^{77–88} also showed positive cooperativity with a correlation of $r^2=0.85$. The intercept with the x -axis indicated that half saturation occurred at 363 μM pep^{77–88} and that the Hill coefficient (n) was approximately 7, indicating again that the Tim8–Tim13 complex has multiple binding sites. In addition, this region of Tim23 seems to induce an increased binding affinity in the Tim8–Tim13 complex.

The positive cooperativity implies that binding at one site of the complex may influence binding at other sites. Further support of this concept comes from two additional experiments. In the first approach, we mixed a fixed concentration of pep^{91–103} with a peptide that has a low binding affinity (pep^{136–148}) to determine whether binding

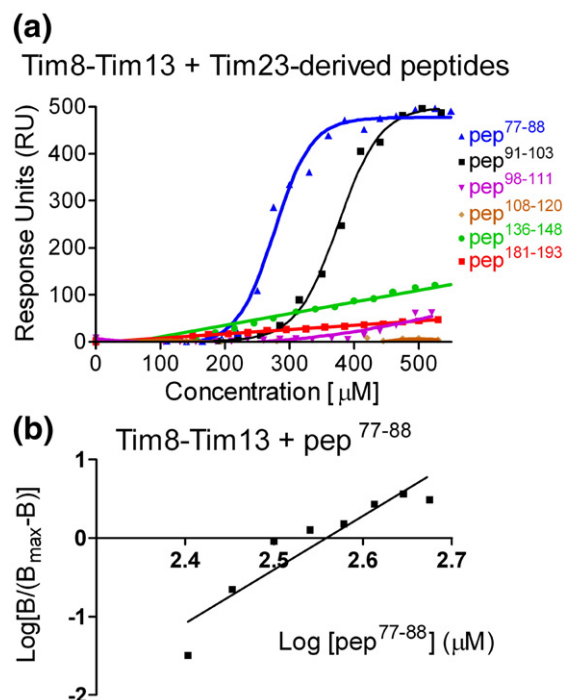


Fig. 5. The Tim8–Tim13 complex displayed different binding properties with different peptides derived from regions of Tim23. (a) Peptides derived from Tim23 (see Fig. 2b) were analyzed for binding to the coupled Tim8–Tim13 complex. The saturation curve was plotted. (b) Binding between pep^{77–88} from (a) was analyzed by the Hill equation as described in Fig. 4c.

by pep^{91–103} could influence the binding of other peptides. A constant low concentration of pep^{91–103} (63 μ M) that could slightly induce binding was added with increasing amounts of pep^{136–148}, and the saturation curve was plotted (Fig. 6a). For comparison, the binding of pep^{136–148} alone was included on the plot. The addition of pep^{91–103} with pep^{136–148} clearly increased the binding of pep^{136–148} approximately three times above that of pep^{136–148} alone. After analysis of the data, the binding interaction was fitted to a first-order binding interaction. The equilibrium dissociation constant

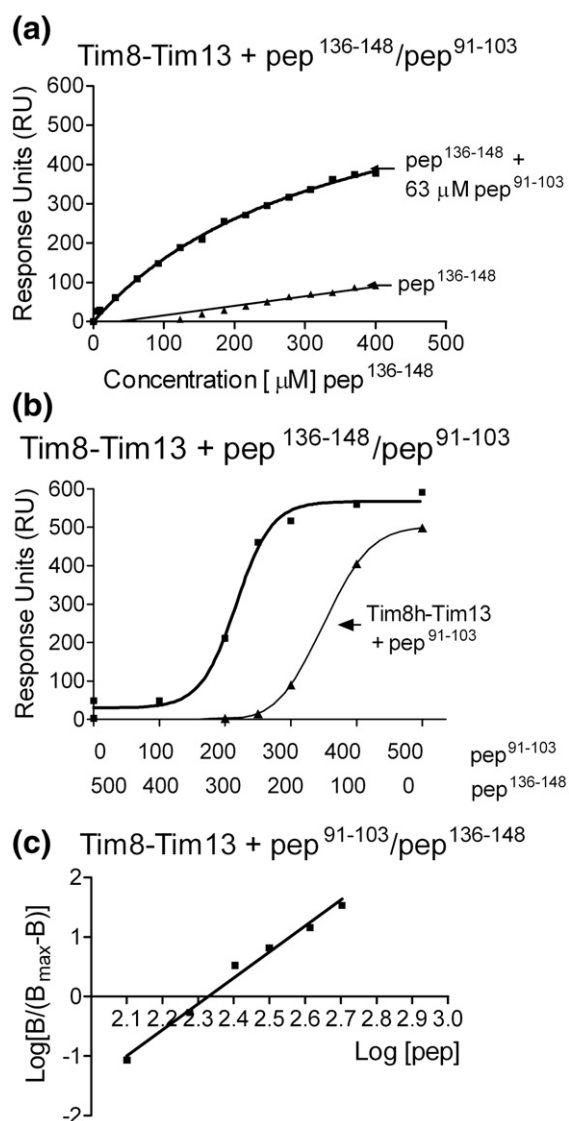


Fig. 6. The addition of pep^{91–103} increased the binding affinity of Tim8–Tim13 for pep^{136–148}. (a) Pep^{91–103} was maintained at a constant concentration of 63 μ M, and pep^{136–148} was added over a range of 0–400 μ M in the buffer (designated pep^{136–148} + 63 μ M pep^{91–103}). Binding to the Tim8–Tim13 complex was measured. The binding curve for pep^{136–148} alone was included for reference. (b) The concentrations of pep^{91–103} and pep^{136–148} were varied inversely such that the total concentration was fixed at 500 μ M in the SPR analysis with Tim8–Tim13. The binding of pep^{91–103} alone was included for reference. (c) The data from (b) were plotted using the Hill equation as in Fig. 4c.

K_d was 350 μ M. In the second assay, we kept the total peptide concentration constant at 500 μ M and inversely varied the pep^{91–103}/pep^{136–148} ratio (Fig. 6b). The saturation curve was plotted, and the saturation curve for pep^{91–103} was included for comparison. Inverting the ratio of the peptides resulted in a sigmoidal curve that showed an affinity for binding higher than that with pep^{91–103} alone. The interaction was plotted using the Hill equation ($r^2=0.97$) (Fig. 6c). The half saturation was 212 μ M, and the Hill coefficient (n) was approximately 4. The binding stoichiometry of approximately 1 Tim8–Tim13 complex:5.9–6.8 peptides was calculated from Eq. (1). In addition to pep^{91–103} enhancing pep^{136–148} binding (Fig. 6a), it seems that binding of pep^{136–148} enhances binding of pep^{91–103} (Fig. 6b). Thus, the Tim8–Tim13 complex displays a different binding affinity, depending on the presence of different peptides, thereby implying that the Tim8–Tim13 complex may undergo conformational changes as a substrate is being bound, allowing it to bind multiple regions of the incoming substrate.

Discussion

Previous studies employing crosslinking and peptide scans suggest that the Tim8–Tim13 complex binds to substrates to shield the hydrophobic regions in the aqueous intermembrane space and that the complex may contact several sites in the substrate.^{4,9,13} Our study builds on these previous reports by determining the structure of the Tim8–Tim13 complex and by addressing the mechanism by which the Tim8–Tim13 complex may bind to substrates. As expected, the Tim8–Tim13 structure is similar to that of Tim9–Tim10; however, the organization of the tentacles with respect to the positions and lengths of their terminal helices differed between the two complexes. This difference may be important for determining substrate specificity.

We have used SPR technology to investigate the interactions with the Tim8–Tim13 complex. We predicted that the central region (amino acids 80–110) of Tim23 most likely entered the intermembrane space first because constructs with dihydrofolate reductase molecules appended to the N- and C-termini of Tim23, which block translocation across the TOM complex, were crosslinked to Tim8 and Tim13, demonstrating that this region has entered the intermembrane space. Studies by Alder *et al.* also showed prevalent crosslinking of the Tim8–Tim13 complex to Tim23 in the same region.¹³ As expected when the complex is composed of six subunits (each with the ability to bind the substrate), the Tim13 monomer showed a typical bimolecular interaction, with the peptide derived from the aforementioned region of Tim23, pep^{91–103}. However, the dissociation constant ($K_d=613$ μ M) indicated that the interaction was of low affinity compared to that of the Tim8–Tim13 complex ($K_d=393$ μ M).

We investigated the binding of the Tim8–Tim13 complex and predicted that the Tim8–Tim13

complex should have multiple binding sites because the complex contains three Tim13 monomers and three Tim8 monomers. Indeed, SPR analysis showed that the complex contains approximately six binding sites. The binding, however, was not a simple bimolecular interaction. The Tim8–Tim13 complex's interaction with the substrate was cooperative for peptides derived from amino acids 77–103 of Tim23, whereas the complex did not bind appreciably to peptides from the C-terminus of Tim23. We suggest that the Tim8–Tim13 complex may undergo a conformational change in which the complex has increased affinity for the substrate. Thus, the central region of Tim23 (amino acids 77–103) may serve as a nucleation point to induce the complex to bind to the

substrate, preparing it for transport across the intermembrane space.

The quick on-rates and off-rates may reflect properties of the Tim8–Tim13 complex interacting with the substrate because the complex binds to the Tim23 substrate as it enters the intermembrane space and then releases it to the insertion complex in the inner membrane. The specific mechanism by which the small Tim complexes release the substrate is not understood.¹ The small Tim proteins do not have an ATP requirement like other chaperones, but release of the substrate at the inner membrane may be due to increased affinity for the Tim22 insertion complex or oxidation–reduction chemistry. Alternatively, there may be an internal timing mechanism

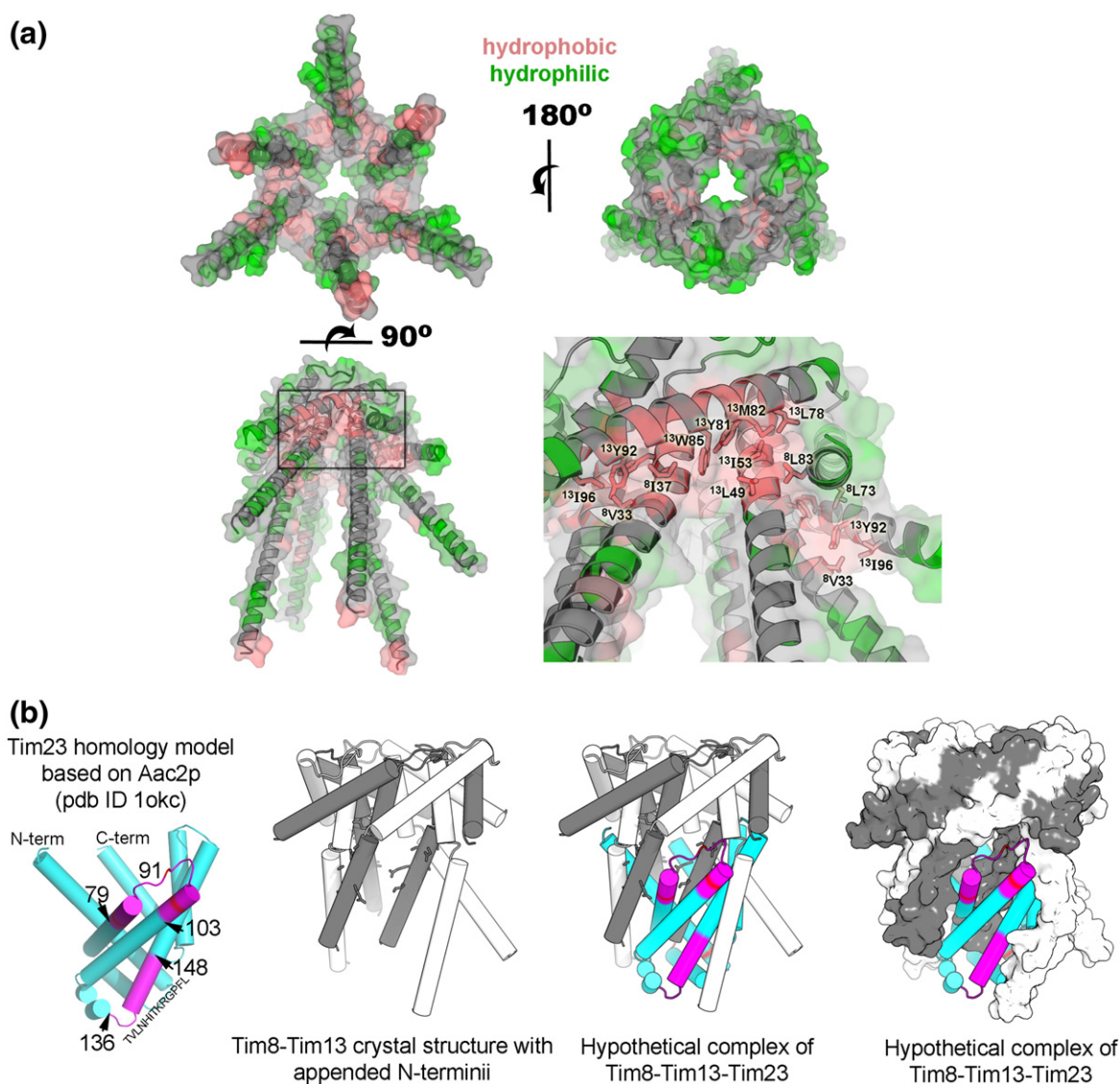


Fig. 7. Model showing the Tim8–Tim13 complex binding to Tim23. (a) Surface hydrophobicity diagrams of the Tim8–Tim13 complex. The hydrophobic residues are shown in pink, and hydrophilic residues are shown in green. N- and C-terminal residues disordered in the Tim8–Tim13 structure are modeled here as α -helices. (b) Model proposing how Tim8–Tim13 binds to the Tim23 substrate. Tim23 folding is based on a weak level of homology to AAC2. Magenta color segments correspond to peptide sequences shown to bind Tim8–Tim13, and dark magenta segments mark conserved residues that are predicted to bind to the substrate. Evolutionarily conserved residues in Tim13 Ile37, Glu40, Ala42, Ala44, Asn45, Ala46, and Leu49 are represented as sticks (see Discussion for details).

such that, as soon as the binding sites in the Tim8–Tim13 complex are loaded, the complex may quickly switch conformations to unload the substrate.

Molecular model of Tim8–Tim13 binding to Tim23

Our structural and binding data suggest a model for the binding of the Tim8–Tim13 complex to Tim23 that differs from that proposed for the binding of the Tim9–Tim10 complex to the AAC complex.¹⁷ In the Tim9–Tim10 model, Tim9 subunits are successively displaced from the hexameric complex as the transmembrane-spanning helices of AAC compete for interaction with the remaining Tim10 subunits. Thus, dissociation of the hexameric barrel is a central feature of the chaperone mechanism. On the contrary, evidence that Tim8–Tim13 binds cooperatively to six Tim23 peptide molecules suggests instead that the Tim8–Tim13 complex does not dissociate, but acts cooperatively, to bind multiple distinct sites on a single Tim23 molecule. To test whether such a mechanism was feasible in terms of accommodating a molecule of 23 kDa within the circumference of the Tim8–Tim13 tentacles, we constructed a model of Tim23 and investigated how it might fit with the Tim8–Tim13 crystal structure. The model of Tim23 is based on a weak sequence similarity with AAC2 using the program Modeller (Fig. 7b),²⁷ but its accuracy is important here only in so much as it reflects the true dimensions and secondary structure content. The dimensions of Tim23 (cyan) fit well, wedged within the N-terminal helical tentacles of the Tim8–Tim13 complex (gray). The Tim23 model like AAC2 has a pseudo-3-fold rotational symmetry that coincides with the 3-fold symmetry of the Tim8–Tim13 complex. Additionally, the regions that are implicated to bind to the Tim8–Tim13 complex (amino acids 79–89, 91–103, and 136–148; marked in magenta) contact the Tim8–Tim13 complex. Notably, Trp93, which derives from the strongest binding of the Tim23 pep^{91–103}, neatly tucks into a pocket formed by Tim8 (Leu73) and Tim13 (Tyr92). At this stage of analysis, nonhydrophobic interactions most likely plan an important role in substrate binding. Gentle *et al.* have used bioinformatics to identify residues Ile37, Glu40, Ala42, Ala44, Asn45, Ala46, and Leu49 as conserved among different Tim13 species.²⁸ These residues have been highlighted by sticks in our model in Fig 7b, and these conserved residues are largely in contact with the modeled Tim23 substrate. By combining the structural analysis with the binding studies, the Tim8–Tim13 complex most likely encompasses one Tim23 monomer (making contact at several sites) to create a system in which the hydrophobic substrate can be escorted to the inner membrane. This model begins to define how the Tim8–Tim13 complex interacts with its substrates.

It is also possible that the Tim8–Tim13 binds to other substrates such as AAC and porin. However, our modeling attempts were not successful (data not shown) because of incompatibilities in the sizes and

charges of amino acid side chains at the proposed region of contact at the helical ring (Tim13 residue W85; Fig. 7a). From crosslinking studies with radiolabeled AAC precursor, a direct interaction between Tim8 and Tim13 has also not been detected,⁷ so the biochemical evidence does point towards specificity in interactions between the Tim8–Tim13 complex and substrates. Porin is a β -barrel protein and, therefore, has a shape different from those of Tim23 and AAC. Experiments pointing to freezing substrate–complex interactions for structural studies are ultimately required to determine how the Tim8–Tim13 complex binds to its substrates.

Materials and Methods

Instrumentation and reagents

All experiments were performed using a BIACORE T100 biosensor developed by BIACORE AB. Series S NTA sensor chips and coupling reagents were also purchased from BIACORE AB.

Peptides, plasmids, and strains

For structural studies, recombinant Tim8–Tim13 complex from *S. cerevisiae*, which lacked affinity tags, was constructed and purified as described previously.⁴ For SPR studies, *TIM13* was cloned into pET28a (Novagen) with a C-terminal 10 \times histidine tag to generate recombinant Tim13. For the Tim8–Tim13 complex for SPR studies, *TIM8* was cloned into pET28a with a C-terminal 10 \times histidine tag as NcoI/SalI fragment, and *TIM13* was cloned into pET28a as NcoI/NdeI fragment. *TIM13* with the ribosomal binding site was then removed as XbaI/NheI fragment and cloned into the XbaI site of the pET28a-TIM8His plasmid. As a result, a single transcript in which both Tim8 and Tim13 were translated from their own ribosomal binding site was synthesized.

His-tagged recombinant proteins were purified using Ni²⁺-NTA agarose. The Tim8–Tim13 complex was purified under native conditions, whereas Tim13 was purified under denaturing conditions in the presence of 8.0 M urea. Assembly of the proteins was tested by blue native PAGE, as described previously.⁴ The purified proteins were dialyzed in TBST buffer (5 mM Tris pH 7.4, 150 mM KCl, and 0.05% Tween-20) overnight at 4 °C. Tim23 peptides for the SPR studies were selected from peptide scan results with the Tim8–Tim13 complex and synthesized by United Biochemical Research (Seattle, WA) at 95% purity (Table 1).⁴ Because of solubility problems, charged residues were added to the N-terminus in peptides that were predicted to have poor solubility in aqueous solution. The addition of the charged residues did not affect the binding studies. The peptides are designated according to the amino acids numbers in the Tim23 protein from *S. cerevisiae*.

Crystallization

The purified Tim8–Tim13 complex was concentrated in a Centricon 10 device (Millipore), and the buffer was exchanged three times with 10 mM Tris (pH 8.0), 10 mM

NaCl, and 3% 2-methyl-2,4-pentanediol. The addition of 2-methyl-2,4-pentanediol to the protein buffer was important in preventing phase separation at high protein concentration. The final protein concentration (30 mg/ml) was measured using absorbance reading at a wavelength of 280 nm (extinction coefficient $\epsilon=10,010 \text{ M}^{-1} \text{ cm}^{-1}$).

Crystals were prepared by mixing 2.0 μl of protein with 2.0 μl of reservoir solution in a sitting-drop vapor-diffusion tray at room temperature. The reservoir solution contained 25% polyethylene glycol 2000 MME and 0.11 M 4-morpholineethanesulfonic acid (pH 6.5). Rhomboid-shaped crystals appeared after 2 weeks. The ability to obtain these crystals varied with different protein preparations. The largest of these crystals was only about 50 μm on edge. The crystals belong to space group *P1*, with cell dimensions very close to a primitive hexagonal (see Table 2 below). Crystals were cryoprotected by a quick swipe through a solution containing 75% reservoir solution and 25% glycerol.

Data collection

X-ray diffraction data to 2.3 \AA were collected at Advanced Light Source beamline 8.2.2 using an ADSC Quantum 315 3 \times 3 charge-coupled device array. Three hundred sixty 1.0 $^\circ$ oscillation frames were collected at a wavelength of 0.9792 \AA . Data reduction and scaling were performed using DENZO/SCALEPACK.²⁹ The diffraction was strongly anisotropic, extending to 2.5 \AA in the a^* and b^* directions, but extending only by 3.1 \AA in the c^* direction. To eliminate the poorly measured reflections between 3.1 and 2.5 \AA , ellipsoidal truncation was performed in accordance with the procedure outlined in Strong *et al.*³⁰ Structure factors whose position on the reciprocal lattice fell outside an ellipsoid (with principle axes of 2.5 \AA^{-1} in the a^* and b^* directions and 3.1 \AA^{-1} in the c^* direction) were eliminated.

Structure determination and refinement

Solving the phase problem by using heavy-atom derivative was foreseen to be extremely challenging for these small and poorly reproducible crystals. Difficulties in producing a sufficient quantity of selenomethionyl derivative prevented us from obtaining phases by multi-wavelength anomalous dispersion. Following the publication of the Tim9–Tim10 complex,¹⁷ the structure could be solved with molecular replacement, using the program Phaser.³¹ A homology model of the Tim8–Tim13 heterohexamer was created by SWISS-MODEL³² based on the crystal structure of the human Tim9–Tim10 heterohexamer [Protein Data Bank (PDB) code 2BSK].¹⁷ The sequence alignments are shown in Fig. 1. Unexpectedly, the homology model produced better rotation and translation function Z-scores than did the crystallographic coordinates of the Tim9–Tim10 complex; a low success rate is typical of the use of homology models in molecular replacement when the template sequence identity is 30% or less.^{33,34} SWISS-MODEL was capable of producing a sufficiently accurate alignment in this case.

First, refinement steps were performed with CNS,³⁵ using simulated annealing and conjugate gradient algorithms, and with the aid of a hydrogen bond potential function.³⁶ Six-fold noncrystallographic symmetry restraints were used throughout (i.e., there were two heterohexamers in the asymmetric unit; six copies of Tim8 were restrained to be geometrically similar to each other, and six copies of Tim13 were similarly restrained). After

each refinement step, the model was visually inspected in Coot,³⁷ using both $2F_o - F_c$ and $F_o - F_c$ difference maps. All hydrogen atoms connected to carbon atoms and backbone nitrogen atoms were included at their geometrically calculated positions and refined using a riding model. The hydrogen atoms provide a useful constraint to prevent violation of van der Waals contacts and do not contribute to F_{calc} . Later rounds of refinement were performed with REFMAC5 to benefit from TLS parameterization of domain disorder.^{38,39} The model was validated with the following structure validation tools: PROCHECK, ERRAT, and VERIFY3D.⁴⁰

Model of the Tim8–Tim13 complex bound to Tim23

First, a model of the Tim23 protein was constructed with the program Modeller,²⁷ since there are no published structures of Tim23 to date. The sequence alignments between Tim23 and potential structural templates were very weak. One of the suggested templates corresponded to bovine AAC protein (AAC2) (PDB code 1OKC). It was selected because AAC2 is known to be a substrate of Tim9–Tim10 complex. Since Tim8–Tim13 is structurally similar to Tim9–Tim10, it seems plausible that their substrates might resemble each other. Furthermore, the AAC2 has a pseudo-3-fold rotational symmetry that conveniently coincides with the 3-fold symmetry of the Tim8–Tim13 complex. Docking the Tim23 model to the Tim8–Tim13 crystal structure was accomplished with the graphics program "O."⁴¹ The N- and C-terminal helices of Tim8–Tim13 were adjusted to fit around the Tim23 molecule, interacting with the transmembrane helices. The loops that connect Tim23 helices fit neatly into hydrophobic pockets where the N- and C-terminal helices of Tim8–Tim13 branch away from the barrel. The model was energy-minimized using CNS.³⁵

CD analysis

CD analysis was performed on a JASCO J-600 spectropolarimeter. A scan speed of 10 nm/min, a time constant of 4 s, and a bandwidth of 1.0 nm were used to acquire the data. In addition to baseline correction, three scans were averaged for each spectrum. The proteins were scanned from 260 to 200 nm at 4 $^\circ\text{C}$ in a 1-mm pathlength cell with protein concentrations of 0.2–0.4 mg/ml. Spectra were analyzed for secondary structure using the convex constraint algorithm for secondary structure prediction.⁴²

SPR analysis

Recombinant Tim8–Tim13 complex and Tim13 monomer were immobilized on the SPR Ni^{2+} chip at 25 $^\circ\text{C}$.⁴³ The chip was activated by injecting 1 mM NiCl_2 over the chip for 2 min at 5 $\mu\text{l}/\text{min}$. Protein in TBST buffer at 6 μM for Tim8–Tim13 complex and at 9.8 μM for Tim13 monomer was immobilized on the chip with two sequential 30-min injections at 5 $\mu\text{l}/\text{min}$ to yield 3500–4000 RU for the Tim8–Tim13 complex and 1500 U for the Tim13 monomer. Note that these concentrations were selected as recommended by the BIACORE website, with the assumption that up to six substrate binding sites may be present on the Tim8–Tim13 complex because it consists of three Tim8 monomers and three Tim13 monomers. Mock-derivatized flow cells served as reference surfaces, and nonspecific binding was subtracted.

The binding analysis was performed at 25 °C and 30 μ l/min flow rate in TBST buffer. Peptides in TBST buffer at concentrations of 0–630 μ M were analyzed for binding to the sensor chip coupled with Tim8h–Tim13 or Tim13h. Binding ran for 25 s, followed by at least 3 min of dissociation phase to allow the baseline to return to the starting level. The chip was typically regenerated with fresh complex after one to two concentration series of a particular peptide.

SPR data for each concentration of peptide were, at minimum, duplicated. Control experiments were conducted to ensure that mass transport and bulk flow limitations were absent in the analyte regime. In addition, Eq. (1) was used to calculate binding stoichiometry between the peptide and the coupled protein²⁵ (MW_r , molecular mass). The Tim8–Tim13 complex has a molecular mass of 63.2 kDa, and the Tim13 monomer has a molecular mass of 12.4 kDa:

$$\text{Binding Stoichiometry} = \frac{RU_{\max}/RU\text{-bound complex}}{MW \text{ peptide}/MW \text{ complex}} \quad (1)$$

The binding data for the Tim8–Tim13 complex were not analyzed kinetically with the Biaevaluation 3.0 software. Attempts at kinetic analysis were unsuccessful because the on-rate proceeded too quickly.²⁶ Therefore, equilibrium binding analysis was employed to analyze the interaction. Furthermore, Tim8–Tim13 and pep^{91–103} were not fitted with either the Biaevaluation 3.0 or the Scrubber-2 software because simple models involving noncooperative interactions could not explain the clearly sigmoidal data. Accordingly, the data were analyzed with a Hill plot with GraphPad Prism 4 to generate a linear fit of the Tim8–Tim13 data set. A Boltzmann sigmoidal curve was generated with GraphPad Prism 4 as a theoretical fit of the data.⁴⁴

Blue native gel electrophoresis

Wild-type mitochondria and recombinant proteins were solubilized (20 mM Hepes, 50 mM NaCl, 10% glycerol, 2.5 mM MgCl₂, 1 mM ethylenediaminetetraacetic acid pH 7.4, and 0.2% *n*-dodecylmaltoside) at 4 °C for 30 min. The lysate was centrifuged at 14,000 rpm for 30 min at 4 °C to pellet any insoluble material. The solubilized proteins were analyzed via blue native gel electrophoresis on a 6–16% linear polyacrylamide gradient.²⁴

Accession code

The coordinates of the final model and the merged structure factors have been deposited with the PDB. The corresponding PDB code is 3CJH.

Acknowledgements

We thank Dr. Martin Phillips (University of California, Los Angeles) for technical assistance with the instrumentation, the UCLA-DOE X-ray Core Technology Center for X-ray crystallography experiments and modeling analysis, and Dr. Steven Claypool for critical reading of the manuscript. C.M.

K. is an established investigator of the American Heart Association. This work was supported by grants from the National Institutes of Health (United States Public Health Service National Service Award GM070404 to K.N.B., 1R01GM61721 to C.M.K., and 23616-002-06 to M.R.S.), the Department of Energy (DE-FC03-02ER63421 to M.R.S.), and the American Heart Association (0640076N to C.M.K.).

Supplementary Data

Supplementary data associated with this article can be found, in the online version, at [doi:10.1016/j.jmb.2008.07.069](https://doi.org/10.1016/j.jmb.2008.07.069)

References

- Koehler, C. M. (2004). New developments in mitochondrial assembly. *Annu. Rev. Cell Dev. Biol.* **20**, 309–335.
- Mokranjac, D. & Neupert, W. (2005). Protein import into mitochondria. *Biochem. Soc. Trans.* **33**, 1019–1023.
- Bohnert, M., Pfanner, N. & van der Laan, M. (2007). A dynamic machinery for import of mitochondrial precursor proteins. *FEBS Lett.* **581**, 2802–2810.
- Curran, S. P., Leuenberger, D., Schmidt, E. & Koehler, C. M. (2002). The role of the Tim8p–Tim13p complex in a conserved import pathway for mitochondrial polytopic inner membrane proteins. *J. Cell Biol.* **158**, 1017–1027.
- Wiedemann, N., Pfanner, N. & Ryan, M. T. (2001). The three modules of ADP/ATP carrier cooperate in receptor recruitment and translocation into mitochondria. *EMBO J.* **20**, 951–960.
- Kovermann, P., Truscott, K. N., Guiard, B., Rehling, P., Sepuri, N. B., Muller, H. *et al.* (2002). Tim22, the essential core of the mitochondrial protein insertion complex, forms a voltage-activated and signal-gated channel. *Mol. Cell*, **9**, 363–373.
- Leuenberger, D., Bally, N. A., Schatz, G. & Koehler, C. M. (1999). Different import pathways through the mitochondrial intermembrane space for inner membrane proteins. *EMBO J.* **17**, 4816–4822.
- Davis, A. J., Sepuri, N. B., Holder, J., Johnson, A. E. & Jensen, R. E. (2000). Two intermembrane space TIM complexes interact with different domains of Tim23p during its import into mitochondria. *J. Cell Biol.* **150**, 1271–1282.
- Davis, A. J., Alder, N. N., Jensen, R. E. & Johnson, A. E. (2007). The Tim9p/10p and Tim8p/13p complexes bind to specific sites on Tim23p during mitochondrial protein import. *Mol. Biol. Cell*, **18**, 475–486.
- Roesch, K., Hynds, P. J., Varga, R., Tranebjaerg, L. & Koehler, C. M. (2004). The calcium-binding aspartate/glutamate carriers, citrin and aralar1, are new substrates for the DDP1/TIMM8a–TIMM13 complex. *Hum. Mol. Genet.* **13**, 2101–2111.
- Hoppins, S. C. & Nargang, F. E. (2004). The Tim8–Tim13 complex of *Neurospora crassa* functions in the assembly of proteins into both mitochondrial membranes. *J. Biol. Chem.* **279**, 12396–12405.
- Curran, S. P., Leuenberger, D., Oppliger, W. & Koehler, C. M. (2002). The Tim9p–Tim10p complex binds to the transmembrane domains of the ADP–ATP carrier. *EMBO J.* **21**, 942–953.

13. Alder, N. N., Sutherland, J., Buhring, A. I., Jensen, R. E. & Johnson, A. E. (2007). Quaternary structure of the mitochondrial TIM23 complex reveals dynamic association between Tim23p and other subunits. *Mol. Biol. Cell*, **19**, 159–170.
14. Walton, T. A. & Sousa, M. C. (2004). Crystal structure of Skp, a prefoldin-like chaperone that protects soluble and membrane proteins from aggregation. *Mol. Cell*, **15**, 367–374.
15. Siegert, R., Leroux, M. R., Scheufler, C., Hartl, F. U. & Moarefi, I. (2000). Structure of the molecular chaperone prefoldin: unique interaction of multiple coiled coil tentacles with unfolded proteins. *Cell*, **103**, 621–632.
16. Hartl, F. U. & Hayer-Hartl, M. (2002). Molecular chaperones in the cytosol: from nascent chain to folded protein. *Science*, **295**, 1852–1858.
17. Webb, C. T., Gorman, M. A., Lazarou, M., Ryan, M. T. & Gulbis, J. M. (2006). Crystal structure of the mitochondrial chaperone TIM9.10 reveals a six-bladed alpha-propeller. *Mol. Cell*, **21**, 123–133.
18. Jones, T. A., Zou, J. Y., Cowan, S. W. & Kjeldgaard, M. (1991). Improved methods for building protein models in electron density maps and the location of errors in these models. *Acta Crystallogr. Sect. A*, **47**, 110–119.
19. Perczel, A., Park, K. & Fasman, G. D. (1992). Analysis of the circular dichroism spectrum of proteins using the convex constraint algorithm: a practical guide. *Anal. Biochem.* **203**, 83–93.
20. Nieba, L., Nieba-Axmann, S. E., Persson, A., Hamalainen, M., Edebratt, F., Hansson, A. *et al.* (1997). BIACORE analysis of histidine-tagged proteins using a chelating NTA sensor chip. *Anal. Biochem.* **252**, 217–228.
21. Wyman, J. & Gill, S. J. (1990). *Binding and Linkage: Functional Chemistry of Biological Macromolecules*. University Science Books, Mill Valley, CA.
22. Matthews, B. W. (1968). Solvent content of protein crystals. *J. Mol. Biol.* **33**, 491–497.
23. Brünger, A. T. (1992). Free R value: a novel statistical quantity for assessing the accuracy of crystal structures. *Nature*, **355**, 472–475.
24. Clamp, M., Cuff, J., Searle, S. M. & Barton, G. J. (2004). The Jalview Java alignment editor. *Bioinformatics*, **20**, 426–427.
25. DeLano, W. L. (2002). *The PyMOL Molecular Graphics System*. DeLano Scientific, San Carlos, CA.
26. Lundin, V. F., Stirling, P. C., Gomez-Reino, J., Mwenifumbo, J. C., Obst, J. M., Valpuesta, J. M. *et al.* (2004). Molecular clamp mechanism of substrate binding by hydrophobic coiled-coil residues of the archaeal chaperone prefoldin. *Proc. Natl Acad. Sci. USA*, **101**, 4367–4372.
27. Martin-Benito, J., Gomez-Reino, J., Stirling, P. C., Lundin, V. F., Gomez-Puertas, P., Boskovic, J. *et al.* (2007). Divergent substrate-binding mechanisms reveal an evolutionary specialization of eukaryotic prefoldin compared to its archaeal counterpart. *Structure*, **15**, 101–110.
28. Schagger, H., Cramer, W. A. & von Jagow, G. (1994). Analysis of molecular masses and oligomeric states of protein complexes by blue native electrophoresis and isolation of membrane protein complexes by two-dimensional native electrophoresis. *Anal. Biochem.* **217**, 220–230.
29. Morton, T. A. & Myszka, D. G. (1988). Kinetic analysis of macromolecular interactions using surface plasmon resonance biosensors. *Methods Enzymol.* **295**, 268–294.
30. Karaveg, K., Siriwardena, A., Tempel, W., Liu, Z. J., Glushka, J., Wang, B. C. *et al.* (2005). Mechanism of class 1 (glycosylhydrolase family 47) [alpha]-mannosidases involved in N-glycan processing and endoplasmic reticulum quality control. *J. Biol. Chem.* **280**, 16197–16207.
31. Eswar, N., John, B., Mirkovic, N., Fiser, A., Ilyin, V. A., Pieper, U. *et al.* (2003). Tools for comparative protein structure modeling and analysis. *Nucleic Acids Res.* **31**, 3375–3380.
32. Gentle, I. E., Perry, A. J., Alcock, F. H., Likic, V. A., Dolezal, P., Ng, E. T. *et al.* (2007). Conserved motifs reveal details of ancestry and structure in the small TIM chaperones of the mitochondrial intermembrane space. *Mol. Biol. Evol.* **24**, 1149–1160.
33. Otwinowski, Z. & Minor, W. (1997). Processing of X-ray diffraction data collected in oscillation mode. *Methods Enzymol.* **276**, 307–326.
34. Strong, M., Sawaya, M. R., Wang, S., Phillips, M., Cascio, D. & Eisenberg, D. (2006). Toward the structural genomics of complexes: crystal structure of a PE/PPE protein complex from *Mycobacterium tuberculosis*. *Proc. Natl Acad. Sci. USA*, **103**, 8060–8065.
35. McCoy, A. J., Grosse-Kunstleve, R. W., Adams, P. D., Winn, M. D., Storoni, L. C. & Read, R. J. (2007). Phaser crystallographic software. *J. Appl. Crystallogr.* **40**, 658–674.
36. Schwede, T., Kopp, J., Guex, N. & Peitsch, M. C. (2003). SWISS-MODEL: an automated protein homology-modeling server. *Nucleic Acids Res.* **31**, 3381–3385.
37. Schwarzenbacher, R., Godzik, A., Grzechnik, S. K. & Jaroszewski, L. (2004). The importance of alignment accuracy for molecular replacement. *Acta Crystallogr. Sect. D*, **60**, 1229–1236.
38. Giorgetti, A., Raimondo, D., Miele, A. E. & Tramontano, A. (2005). Evaluating the usefulness of protein structure models for molecular replacement. *Bioinformatics*, **2**, ii72–ii76.
39. Brünger, A. T., Adams, P. D., Clore, G. M., DeLano, W. L., Gros, P., Grosse-Kunstleve, R. W. *et al.* (1998). Crystallography and NMR system: a new software suite for macromolecular structure determination. *Acta Crystallogr. Sect. D*, **54**, 905–921.
40. Fabiola, F., Bertram, R., Korostelev, A. & Chapman, M. S. (2002). An improved hydrogen bond potential: impact on medium resolution protein structures. *Protein Sci.* **11**, 1415–1423.
41. Emsley, P. & Cowtan, K. (2004). Coot: model-building tools for molecular graphics. *Acta Crystallogr. Sect. D*, **60**, 2126–2132.
42. Murshudov, G. N., Vagin, A. A. & Dodson, E. J. (1997). Refinement of macromolecular structures by the maximum-likelihood method. *Acta Crystallogr. Sect. D*, **53**, 240–255.
43. Winn, M. D., Murshudov, G. N. & Papiz, M. Z. (2003). Macromolecular TLS refinement in REFMAC at moderate resolutions. *Methods Enzymol.* **374**, 300–321.
44. Lüthy, R., Bowie, J. U. & Eisenberg, D. (1992). Assessment of protein models with three-dimensional profiles. *Nature*, **356**, 83–85.